Extremely large Seebeck coefficient of gelatin methacryloyl (GelMA)-based thermogalvanic cells by the dual effect of ion-induced crystallization and nanochannel control

Shao-Huan Hong [a, f], Ching-Chieh Hsu [b, f], Tai-Hung Liu [c], Tai-Chou Lee [a],
Shih-Huang Tung [d], Hsin-Lung Chen [e], Jiashing Yu [c, **], Cheng-Liang Liu [b, *]

[a] Department of Chemical and Materials Engineering, National Central University, Taoyuan 32001, Taiwan
[b] Department of Materials Science and Engineering, National Taiwan University, Taipei 10617, Taiwan
[c] Department of Chemical Engineering, National Taiwan University, Taipei 10617, Taiwan
[d] Institute of Polymer Science and Engineering, National Taiwan University, Taipei 10617, Taiwan
[e] Department of Chemical Engineering, National Tsing Hua University, Hsinchu 30013, Taiwan

ARTICLE INFO

ABSTRACT

The quasi-solid state thermogalvanic cells (TGCs) have been extensively investigated due to their high Seebeck coefficient (S) and suitability for wearable power generation. However, the influence of hydrogel nanostructure on Seebeck coefficient remains underexplored. In this study, biocompatible TGCs based on gelatin methacryloyl (GelMA) are fabricated via a fast-photocrosslinking process. Moreover, guanidium chloride (GdmCl) salts are directly introduced into the TGCs to enhance the Seebeck coefficient via ion-induced crystallization in the p-type $FeCN_6^{3-}/FeCN_6^{4-}$ redox system. Small angle X-ray scattering reveals controlled GelMA hydrogel mesh size adjusting the amount of GdmCl, leading to improved intermolecular interactions between the guanidium cations and GelMA polymer. The optimized p-type Seebeck coefficient reaches an unprecedented 21.6 mV K^{-1}, which is the highest thus far reported in the context of the TGC system. Furthermore, a prototype wearable thermoelectric generator (TEG) with an output voltage of 1.6 V under a temperature difference (ΔT) of 9 °C is able to power an LED directly without requiring an additional voltage booster. In brief, the dual effect of ion-induced crystallization and nanochannel control substantially enhances the Seebeck coefficient of the TGC, thereby offering a promising strategy for enhancing the performance of low-grade thermal energy harvesting wearable TEGs.

© 2024 Elsevier Ltd. All rights reserved.

1. Introduction

The global consensus on achieving net zero emissions has spurred widespread research into green and renewable energy solutions in recent years [1,2]. Concurrently, the advancement of technologies such as human sensing and wearable electronics has led to a growing demand for wearable power generation devices [3,4]. Among these devices, wearable thermoelectric systems have attracted significant attention due to their sustainable power generation capabilities, distinguishing them from triboelectric

nanogenerators, piezoelectric nanogenerators, and solar cells [5–8]. By leveraging the Seebeck effect, thermoelectric materials can convert heat differentials into electrical energy. However, conventional inorganic thermoelectric materials are typically designed for high-temperature environments (above 150 °C) and exhibit limited Seebeck coefficients (S) of several hundred μV K^{-1}, thus rendering them less suitable for harnessing low-grade thermal energy such as body heat [9,10]. Furthermore, the intrinsically rigid nature, high cost, toxicity, and complicated processing of inorganic thermoelectric materials impose limitations on their potential applications in wearable energy harvesting [11–13].

By contrast, the thermogalvanic cells (TGCs) have emerged as promising candidates for wearable energy harvesting due to their higher Seebeck coefficients in the order of mV K^{-1} [14,15]. The TGCs operate on the basis of redox reactions occurring at the electrode

surfaces when exposed to a temperature gradient (ΔT), thereby generating a voltage difference (ΔV) and enabling continuous power generation. For instance, Zhou et al. [16] proposed the approach of increasing the entropy difference between redox couples, and demonstrated a concentration gradient between two electrodes via the encapsulation of triiodide ions in α-cyclodextrin (α-CD). As a result, the aqueous α-CD$-I_3^-/I^-$ system achieved a p-type Seebeck coefficient of 2.0 mV K^{-1} (A p-type Seebeck coefficient value in a thermogalvanic system is denoted as a positive symbol in this paper). In 2018, Duan et al. [14] leveraged the ion-induced crystallization effect by the introduction of guanidium chloride (GdmCl) salts and urea into the $FeCN_6^{3-}/FeCN_6^{4-}$ redox solution to obtain liquid TGCs with an enhanced a p-type Seebeck coefficient of 4.2 mV K^{-1}. However, traditional liquid-state TGCs suffer from the drawback of redox solution leakage, which poses challenges in the packaging and construction of modules for wearable devices [17,18]. Consequently, the quasi-solid state TGCs have attracted significant research interest aimed at addressing this issue, and significant efforts have been made to enhance their Seebeck coefficients [11,19−28]. For instance, Han et al. [29] reported the synergistic thermogalvanic and thermodiffusion effects (collectively termed the Soret effect), and achieved an impressive p-type Seebeck coefficient of 17 mV K^{-1} in the KCl$-FeCN_6^{3-}/FeCN_6^{4-}$ gelatin system. In addition, Liu et al. [30] systematically investigated the solvent effect as a strategy for enhancing the Seebeck coefficient, giving an n-type S value of -2.49 mV K^{-1} for the tetramethylene sulfone$-Fe^{2+}/Fe^{3+}$ polyacrylamide hydrogel system. With additive engineering in quasi-solid state TGCs, Zhang et al. [31] in 2022 developed quasi-solid state TGCs using GdmCl salts to make a GdmCl$-FeCN_6^{3-}/FeCN_6^{4-}$ polyacrylamide/sodium alginate dual-network system to achieve a Seebeck coefficient of 4.4 mV K^{-1}. Subsequently, Li et al. [32] achieved a high Seebeck coefficient of 24.7 mV K^{-1} by introducing glutaraldehyde into the synergistic KCl$-FeCN_6^{3-}/FeCN_6^{4-}$ gelatin system. More recently, Zhou et al. [33] fabricated porous gels by utilizing sodium acetate (NaAc) templates and a freeze-drying treatment. By enhancing the mass transfer of electrolytes and introducing the GdmCl salts, the maximum power density of the TGC was increased from 4.01 to 7.68 mW m^{-2} at $\Delta T = 10$ °C. However, in the absence of GdmCl, the pore structure had no apparent effect on the Seebeck coefficient.

Although adjusting the electrolyte solution represents a relatively fast way to improve the thermoelectric performance, there is minimal research exploring the influence of the hydrogel structure (and, particularly, the nanostructural mesh size) on these properties. For example, Jiang et al. [34] reported homogeneous agar gel-electrolyte hydrogels with microscale pore sizes ranging from 1 to 10 μm and an isotropic Seebeck coefficient of 3.3 mV K^{-1}. Nevertheless, the impact of the GdmCl$-FeCN_6^{3-}/FeCN_6^{4-}$ electrolyte on the pore size of the agar hydrogel was not addressed. Consequently, it is essential to comprehend the effects of redox couples and/or additives on the micro- or nano-structures of the hydrogels, as this may induce variations in the Seebeck coefficient. Moreover, the fabrication process of the TGC plays a pivotal role in determining its potential for commercialization, particularly with respect to hydrogel formation. For instance, while chemical crosslinking can enhance the mechanical properties of the hydrogel, the traditional thermal crosslinking process is time-consuming. Furthermore, the use of clean and non-toxic materials and processing methods is crucial for wearable electronic applications.

In the present study, the biocompatible material gelatin methacryloyl (GelMA) is used as the hydrogel matrix for the fabrication of a quasi-solid state TGC via a rapid photocrosslinking process [35,36]. By introducing the GdmCl salts into the TGC, an impressive Seebeck coefficient of 21.6 mV K^{-1} is achieved due to the ion-induced crystallization effect. To the best of the present authors'

knowledge, this represents the highest Seebeck coefficient thus far achieved in the GdmCl$-FeCN_6^{3-}/FeCN_6^{4-}$ system. Moreover, the nanostructure of the GelMA-based hydrogel is systematically analyzed via small angle X-ray scattering (SAXS). The results reveal that the GdmCl salts interact with the GelMA polymers and regulate the mesh size, thereby influencing the mass transfer of the redox couple and ion-induced crystals, ultimately enhancing the entropy of the redox couple. Based on the high Seebeck coefficient, a prototype 9-unit thermoelectric generator (TEG) is demonstrated with an output voltage of about 1.6 V at $\Delta T = 9$ °C, capable of directly powering a light-emitting diode (LED) without the need for a voltage booster. This study highlights the dual effects of ion-induced crystallization and mesh-size control facilitated by the GdmCl salts, which further enhance the Seebeck coefficient. The substantial output voltage, along with the rapid and simplified fabrication process using biocompatible GelMA materials, underscores the potential applications of the GelMA-based hydrogel in wearable TEGs, and offers the feasibility of fabricating TGCs via three-dimensional printing processes.

2. Experimental section

2.1. Synthesis of gelatin methacryloyl (GelMA)

GelMA was synthesized following a previously reported procedure [37,38]. Briefly, precursor A was prepared by dissolving 1 g of gelatin powder in 100 mL of 0.01 M phosphate buffered saline (PBS) solution in deionized (DI) water, and precursor B was prepared separately by dissolving 500 mg of N-succinimidyl methacrylate in 100 mL of dimethylsulfoxide (DMSO). Each precursor was heated at 60 °C for 2 h, after which the two precursors were mixed and cooled overnight in a water bath. The GelMA solution was then purified by dialysis against DI water through a cellulose membrane. Finally, the solution was lyophilized for 3 days, and the GelMA powder was stored in a desiccator at ambient temperature for further use.

The degree of substitution (DS) of the GelMA was determined by ^{1}H nuclear magnetic resonance (^{1}H NMR) spectroscopy (AVIII-500, Bruker) [38,39]. After normalizing the phenylalanine signal (7.0−7.5 ppm), the lysine methylene signals (2.9−3.0 ppm) were integrated to obtain the areas A (lysine methylene of gelatin) and A (lysine methylene of GelMA). The DS of GelMA was then calculated using Eq. (1):

$$DS = \left(1 - \frac{A \text{ (lysine methylene of GelMA)}}{A \text{ (lysine methylene of gelatin)}}\right) \times 100\% \qquad (1)$$

2.2. Fabrication of the quasi-solid-state TGCs

The fabrication of the quasi-solid-state TGCs is illustrated in Fig. 1. Briefly, GelMA powder (15% w/w), GdmCl (0, 1, 3, 5, and 10% w/w) and the photoinitiator Lithium phenyl$-2,4,6-$trimethylbenzoyl$-$Phosphinate (LAP) (2% w/w with respect to GelMA) were dissolved into DI water and heated at 60 °C for 2 h. The solution was then cooled to 40 °C for further use. To prepare the hydrogels, each homogeneous precursor solution was poured into a glass mold ($1.5 \times 1.5 \times 0.5$ cm^3) and crosslinked for 2 min using an ultraviolet (UV) conveyor system with a wavelength of 365 nm and an intensity of 330 mW cm^{-2}. The hydrogels containing 0, 1, 3, 5, and 10% GdmCl were denoted as GelMA_0G, GelMA_1G, GelMA_3G, GelMA_5G, and GelMA_10G, respectively (Fig. 2a). For fabrication of the quasi-solid-state TGCs, the hydrogels were soaked overnight in a mixed solution of 0.4 M K$_3$Fe(CN)$_6$/K$_4$Fe(CN)$_6$ in DI water. The
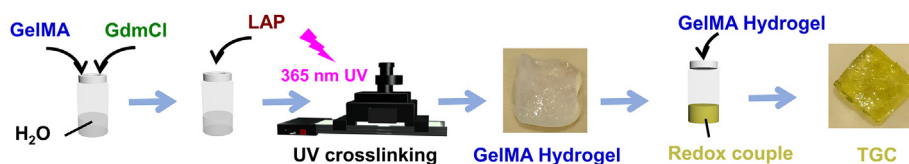
Fig. 1. A schematic diagram showing the fabrication process of the GelMA-based TGCs. The photographic images of GelMA-based hydrogel and TGC are the GelMA_5G hydrogel and TGC, respectively.
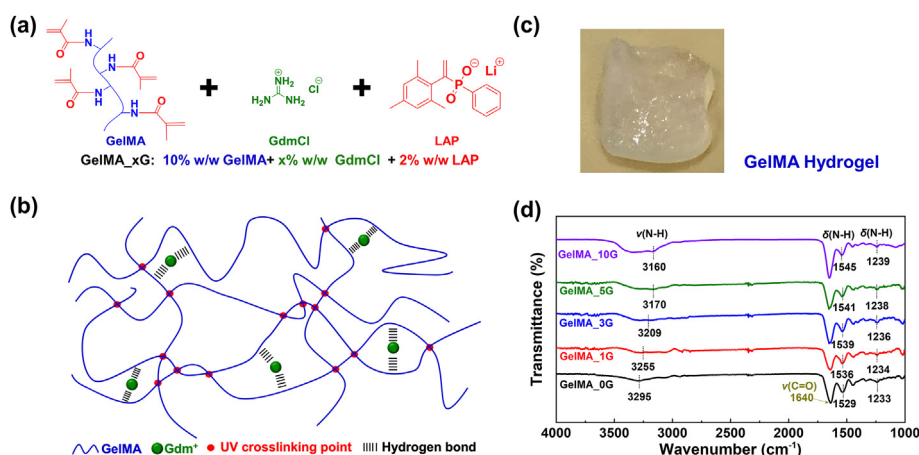

Fig. 2. (a) The chemical structures of GelMA, GdmCl, and LAP. (b) A schematic diagram of the GelMA-based hydrogel network. (c) A photographic image of a GelMA_5G hydrogel. (d) The FT-IR spectra of the freeze-dried GelMA-based hydrogel powder.

TGCs were then obtained by removing the residual redox solution through wipers from the hydrogel surface.

2.3. Fabrication of the wearable thermoelectric generators

To fabricate the wearable thermoelectric generators, either three or nine TGCs were placed in a polydimethylsiloxane (PDMS) mold in a 1 × 3 or 3 × 3 array configuration, respectively. These cells were then connected by nickel foils in a Z-shape configuration, as shown in Fig. 7a. Finally, the thermoelectric generator was encapsulated using thermally conductive adhesive tape and polyimide (PI) tape.

For measurement, the TGC was placed in the middle of two platinum (Pt) electrodes (1.5 × 1.5 cm^2), which were affixed on the surface of heat sinks using PI tape. The temperatures of the hot and cold heat sinks were controlled by a water-cooling system and were varied within the range of 24−34 °C at 80% relative humidity. To measure the temperature, K-type thermocouples were positioned between the Pt electrode and the TGC, and a Keithley DAQ 6510 multimeter was used for data acquisition. The voltage difference across the TGC was measured under each temperature gradient (ΔT) using a Keithley 2182A nanovoltmeter. The Seebeck coefficient was determined by fitting a linear regression to 5−6 data points. Additionally, the Seebeck coefficient of each TGC was calculated based on 5 identically fabricated devices.

The performance of the thermoelectric generator was evaluated using the same setup and orientation, with the exception of using Ni foil as the electrode. The thermoelectric generator was placed in the tested environment for at least 10 min, to make sure both the hot and cold sides of the thermoelectric generator were in equilibrium with the set temperature. The output characteristics were measured by sweeping currents through the device and recording the output voltage at a constant ΔT between the hot and cold heat sinks. The output power was calculated by multiplying the output voltage by the sweeping current. A Keithley 2400 source meter was used to pass current. A thermal camera was employed to detect the temperature of human skin and the surface of the thermoelectric generator when applied to a wearable device worn on the forearm.

3. Results and discussion

The present study presents a novel approach for the fabrication of GelMA hydrogels using GdmCl in a one-step processing method aimed at reducing the additional processing procedures and improving the Seebeck coefficient of the TGCs. The structures of the materials used are shown in Fig. 2a, while the fabrication process of the GelMA-based TGC is shown schematically in Fig. 1, and is detailed in the Experimental section. The process begins by mixing GelMA powder with varying amounts of GdmCl in deionized (DI) water to prepare the precursor solution. A photoinitiator is then added to the solution. The mixing solution is injected into a glass mold and shaped into hydrogels through UV-crosslinking. Subsequently, the GelMA-based hydrogels are soaked in a Fe(CN)$_6^{3-}$/Fe(CN)$_6^{4-}$ solution to create the TGC. The sample name of GelMA-based hydrogels in this research is defined as GelMA_xG, where x is represented the concentration of GdmCl (x = 0, 1, 3, 5, and 10, corresponding to 0, 1, 3, 5, 10% w/w of GdmCl, respectively).

The successful synthesis of GelMA by substituting the amine groups of gelatin with methacryloyl groups is confirmed by a comparison of the ^{1}H NMR spectra of gelatin and GelMA in Figs. S1a and b, respectively [40]. Specifically, the NMR spectrum of GelMA exhibits new peaks at δ = 5.4 and 5.6 ppm due to the acrylic protons of the methacryloyl groups [38], along with a new peak at δ = 1.9 ppm due to the methyl groups of the methacryloyl. Meanwhile, the absence of the signal at δ = 2.9 ppm demonstrates the complete substitution reaction of the lysine methylene moieties [41]. These

observations, along with the nearly 100% DS, clearly demonstrate the successful grafting of methacryloyl groups onto the gelatin.

The formation of the GelMA polymer network via the photo-crosslinking process is shown schematically in Fig. 2b, and confirmed by the photographic image of a GelMA-based hydrogel sample in Fig. 2c. Consistently, the FT-IR spectra of all the as-prepared freeze-dried GelMA-based hydrogels in Fig. 2d and Fig. S2 exhibit characteristic peaks at 3295, 1640, 1529, and 1233 cm^{-1} due to the N−H stretching, the C=O stretching of amide I, the N−H bending of amide II, and the N−H bending of amide III, respectively [42]. The presence of an identical C=O stretching peak in all GelMA-based hydrogels confirms the successful replacement of the amino group by the methacryloyl group. Notably, the N−H stretching peaks are clearly seen to shift significantly towards lower wavenumbers, while the N−H bending peaks shift less strongly towards higher wavenumbers, as the concentration of GdmCl within the hydrogel is increased. These phenomena can be attributed to the weakening of the force constant of the N−H bonds, and the increase in the restoring force, respectively, due to hydrogen bonding between the GelMA polymers and the guanidinium cation (Gdm$^+$) [43,44]. In addition, the pronounced shift in the N−H stretching peak for the GelMA_5G and GelMA_10G can be partially attributed to the presence of GdmCl crystals [45], thereby indicating the formation of stronger intermolecular hydrogen bonds between the GelMA polymer and Gdm$^+$.

The morphologies of the GelMA-based hydrogels are revealed by the cross-sectional scanning electron microscope (SEM) images in Fig. 3, where the microscale pore size is seen to increase initially with the addition of GdmCl (i.e., GelMA_1G compared to GelMA_0G), and to decrease thereafter with the increase in GdmCl concentration. In addition, salts are seen to precipitate on the surface of the GelMA_10G hydrogel. The initial increase in pore size can be attributed to the chaotropic property of the GdmCl salt, which hinders the intermolecular hydrogen bonding between the GelMA polymers and therefore changes the conformation of GelMA. With keeping increasing the concentration of GdmCl, the pore size is then decreased in spite of the chaotropic property is existed. The subsequent reduction in pore size from GelMA_1G to GelMA_10G is consist with the abovementioned FT-IR results, where stronger intermolecular interactions between the GelMA polymer and Gdm$^+$ at higher GdmCl concentrations were accompanied by a larger shift in the N−H stretching peak, while the conformation of GelMA_0G is different with the one of other GelMA_xG hydrogels (x = 1, 3, 5, and 10), this will discuss later.

The strength of hydrogen bonding is also reflected by the mechanical properties of the GelMA-based hydrogels, as revealed by the rheological analysis in Fig. S3. In the sweep mode of oscillation strain, the critical point value, as determined by the intersection of the G′ and G″ curves, is seen to be 50.3%, 103.5%, and 107.7% for the GelMA_0G, GelMA_1G, and GelMA_3G, respectively. However, this value decreases to 96.6% and 92.8% for the GelMA_5G and GelMA_10G hydrogels, respectively, thus indicating the influence of higher GdmCl concentrations. Furthermore, the storage modulus in the strain-independent region increases from 33.1 kPa, through 34.0 kPa, to 49.5 kPa for the GelMA_0G, GelMA_1G, and GelMA_3G, respectively, but then decreases to 38.20 and 37.55 kPa for the GelMA_5G and GelMA_10G, respectively. This suggests that the presence of excess GdmCl, which does not interact with gelatin molecules, leads to a decrease in the mechanical properties of the hydrogel. Overall, the incorporation of Gdm$^+$ in the hydrogel enhances its storage modulus and critical oscillation strain, thus making it suitable for wearable applications.

In addition, the introduction of GdmCl into the GelMA hydrogel offers benefits to the thermogalvanic system using the Fe(CN)$_6^{3-}$/Fe(CN)$_6^{4-}$ redox couple with DI water as the solvent [31,46,47], where the Seebeck coefficient is primarily determined by the concentration gradient (ΔC_r) between the electrodes [31,33,46]. Here, after the reduction reaction of Fe(CN)$_6^{3-}$, the Gdm$^+$ in the GdmCl-added hydrogel selectively interacts with Fe(CN)$_6^{4-}$ to form crystals at the cold side, and this leads to the dissociation of complexes into Gdm$^+$ and Fe(CN)$_6^{4-}$, which then oxidizes to Fe(CN)$_6^{3-}$ at the hot side. In detail, the formation of crystals and the precipitation of complexes lead to an imbalance in the concentration of the redox couple between the cold and hot sides, with a lower concentration of Fe(CN)$_6^{4-}$ near the cold side promoting the reduction reaction, and a higher concentration of Fe(CN)$_6^{4-}$ near the hot side enhancing the oxidation reaction [46]. Therefore, the Seebeck coefficient is improved due to the sustained ΔC_r by this imbalance reaction.

Next, the thermoelectric performance of the GelMA-based TGC was evaluated in the vertically oriented setup (Fig. 4a). In this experiment, each TGC was positioned between Pt electrodes connected to the hot and cold sides, and the thermovoltage (ΔV) was measured under various temperature gradients (ΔT). The Seebeck coefficient (S) was then determined using Eq. (2):

$$S = -\frac{\Delta V}{\Delta T} = -\frac{V_{hot} - V_{cold}}{T_{hot} - T_{cold}} \tag{2}$$
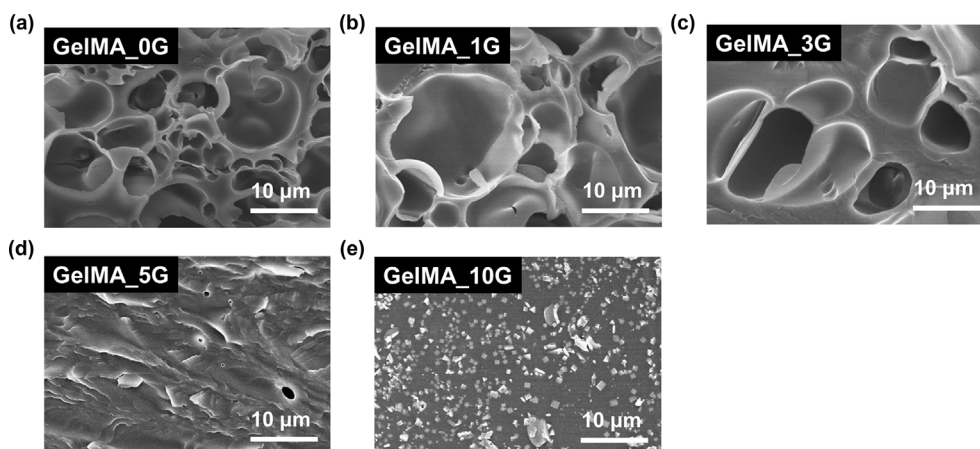

Fig. 3. The SEM images of the freeze-dried of GelMA-based hydrogels: (a) GelMA_0G, (b) GelMA_1G, (c) GelMA_3G, (d) GelMA_5G, and (e) GelMA_10G.
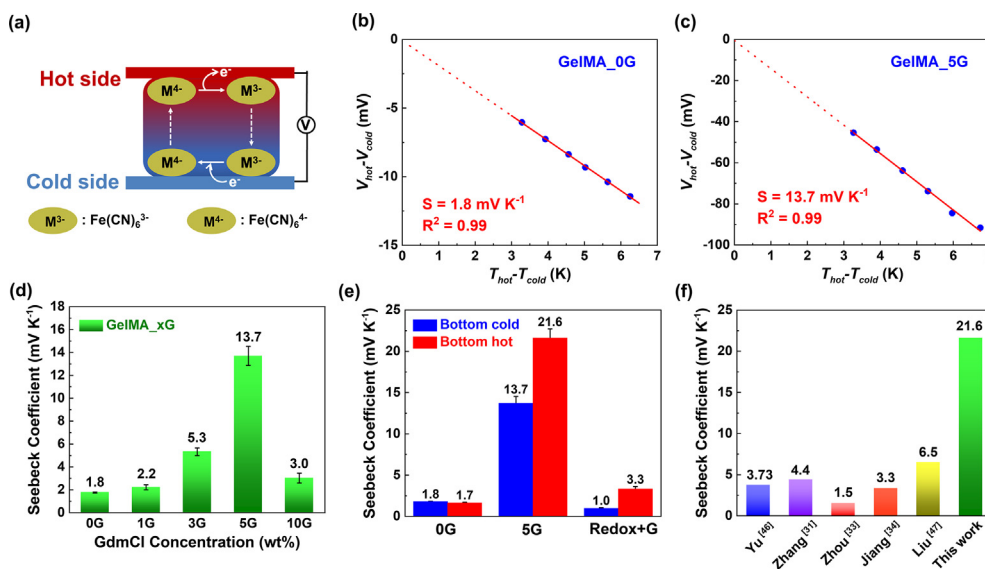
Fig. 4. (a) A schematic diagram of the vertically oriented thermogalvanic system, with the hot side positioned above the cold side; (b and c) the relationship between ΔV and ΔT for (b) the GelMA_0G TGC and (c) the GelMA_5G TGC; (d) the average Seebeck coefficients of the GelMA-based TGCs; (e) the average value of orientation-dependent Seebeck coefficients of the GelMA_0G, the GelMA_5G TGCs, and the GelMA_0G hydrogels after soaking in the redox couple/GdmCl mixed solution; (f) a comparison of the Seebeck coefficients of GelMA_5G TGCs with those of previously-published GdmCl-based TGCs.

where V_{hot}, V_{cold}, T_{hot}, and T_{cold} represent the voltage and temperature of the hot and cold electrodes, respectively. The results are presented in Fig. 4b, c, and S4, where the maximum Seebeck coefficient of the GelMA-based TGC initially increases, and then decreases, as the concentration of GdmCl increases. Compared to the GelMA_0G TGC, the GdmCl-containing devices exhibit higher Seebeck coefficients, with an optimized average value of approximately 13.7 mV K^{-1} for the GelMA_5G TGC (Fig. 4d). In addition, the cyclic voltammetry results in Fig. S5 exhibit clear redox potential peaks for both the GelMA_0G and GelMA_5G TGCs, thereby indicating a reversible redox process suitable for thermogalvanic applications. The presence of an additional broad peak at 0.8 V in the GelMA_5G TGCs might be the signal of ion-induced crystals (Fig. S5b).

To further investigate whether GdmCl salts could contribute the Seebeck coefficient in GelMA-based TGCs, the time-dependent thermoelectric performance of GelMA_5G TGCs was also tested. Fig. S6a shows the four-stage and temporary change in the voltage difference with ΔT (Fig. S6b). For the stage I and II in Fig. S6a, the voltage difference of the GelMA_5G TGC is increased and then remains at a constant value of about 145 mV when ΔT reaches a stable value of 6.5 °C). Throughout the stage III, an external resistance with 10 Ω is connected to the GelMA_5G TGCs. The ΔV decreased rapidly to the value about 10 mV due to the movement of generated electrons from a hot electrode to a cold electrode through the external load, in order to make compensation for the voltage imbalance between two electrodes. Since the thermogalvanic effect exists with a stable temperature difference, the voltage difference could not drop to zero. In the stage IV, when the external load is removed and ΔT keeps at 6.5 °C, the ΔV increased to the value of about 125 mV, which is not the original value. This phenomenon reveals that the giant Seebeck coefficient of the GelMA_5G TGC is mainly determined by the thermogalvanic effect and accompanied by the partial contribution of the thermodiffusion effect from GdmCl ions, since the partial carriers induced by the GdmCl ions are discharged after introducing the external load and could not be charged in the stage IV.

The effects of the processing procedure and measurement setup on the Seebeck coefficients of the various GelMA-based TGCs are revealed by the results in Fig. 4e and S7. With respect to the measurement setup, the Seebeck coefficient of the GelMA_5G TGC is

seen to increase significantly from 13.7 to 21.6 mV K^{-1} when the cold electrode is positioned above the hot electrode compared to the reverse configuration (Figs. S7b and e). This can be attributed to the ion-induced formation of crystals on the cold side, as these spontaneously precipitate to the bottom and dissociate, thereby resulting in a sustained ΔC_r. By contrast, the Seebeck coefficient of the GelMA_0G TGC is almost identical at 1.7 and 1.8 mV K^{-1} in both measurement configurations (Figs. S7a and d), as there is a concentration balance of the redox couple within this hydrogel under stable conditions. With respect to the processing procedure, the devices that were fabricated as described above are compared with those fabricated using the soaking step described by Yu et al. (2020) and Zhang et al. (2022) [31,46], whereby each hydrogel was immersed in the GdmCl/redox mixing solution (3 M GdmCl and 0.4 M Fe(CN)$_6^{3-}$/Fe(CN)$_6^{4-}$). As shown in Figs. S7c and f, the latter devices (designated as the redox + G TGCs) also exhibit a difference in the Seebeck coefficient (1.0 and 3.3 mV K^{-1}, respectively) depending on the measurement configuration, thus further highlighting the effect of ion-induced crystallization. Thus, the overall highest Seebeck coefficient is 21.6 mV K^{-1} for the GelMA_5G TGC (Fig. S7e); this is the highest value ever reported for GdmCl-based TGCs (Fig. 4f), and is comparable to that of 24.7 mV K^{-1} for the synergistic thermodiffusion and thermogalvanic system investigated by Li et al. [32].

To investigate the impact of the nanostructure of the GelMA-based hydrogel on the transport of the redox couple and ion-induced crystals, the hydrogel structure was characterized by small angle X-ray scattering (SAXS). The Beaucage unified equation was then used to analyze the scattering profile and reveal the multi-level structure of the hydrogel [48,49]. This model for the two-level structure of SAXS is given by Eq. (3):

$$I(q) \cong \text{background} + \sum_{i=1}^{N} \left[G_i \exp\left(-\frac{q^2 R_{gi}^2}{3} \right) + B_i \exp\left(-\frac{q^2 R_{g(i+1)}^2}{3} \right) \left(\frac{1}{q_i^*} \right)^{P_i} \right] \tag{3}$$

$$q_i{}^* = q\left[\mathrm{erf}\left(\frac{qR_{gi}}{\sqrt{6}}\right)\right]^{-3}$$

where G_i, B_i, and R_g are the Guinier scaling pre-factor, power law scattering pre-factor, and radius of gyration, respectively. The exponent P_i represents the fractal dimension of level i of the structure, where $i = 1$ and 2 for the global and local structure, respectively. The fitting results for the GelMA-based hydrogels are presented in Fig. 5a, and those of the GelMA_0G and GelMA_5G TGCs before and after soaking in the redox couple are compared in Fig. 5b and c respectively. In all cases, the parametric results are listed in Table S1. Thus, significant differences in the structural parameters are observed upon the addition of GdmCl and upon increasing its concentration. In the middle-to low-q range ($q = 0.004$–0.05 Å^{-1}) in Fig. 5a, all of GelMA-based hydrogels display mass fractal behavior in their global structures, with a mass fractal dimension (P_1) of 2.8, 3.0, 2.8, 2.2, and 1.8 for the GelMA_0G, GelMA_1G, GelMA_3G, GelMA_5G, and GelMA_10G, respectively. Compared to GelMA_0G hydrogels, the larger P_1 values of the GelMA_1G hydrogels may be attributed to the chaotropic properties of the GdmCl salt. The addition of a low concentration of GdmCl to the precursor solution (GelMA_1G) promotes the dispersion of the GelMA powder, thus resulting in a denser hydrogel network in the global structure after photo-crosslinking. At higher GdmCl concentrations, however, micro-phase separation occurs, thus leading to the formation of a looser network and, hence, a decrease in the P_1 values of the GelMA_3G, GelMA_5G and GelMA_10G hydrogels. The phenomenon of micro-phase separation in high-concentration-GdmCl GelMA hydrogels could be proved by SAXS results with q values below 0.004 Å^{-1}. The SAXS patterns of the GelMA_5G and GelMA_10G each exhibit a shoulder at q values below 0.004 Å^{-1}, which may be attributed to the formation of even larger aggregates of GelMA polymers and/or GdmCl salt [50]. However, this region could not be well fitted by including another structural level in the unified equation due to the limitation of the lowest accessible q by the SAXS instrument. The chaotropic behavior of GdmCl and the micro-phase separation in the GelMA-based hydrogels also influence the R_{g1} value, which characterizes the average size of the fractal network. Thus, the R_{g1} value initially decreases from 205.2 Å for the GelMA_0G hydrogel to 134.1 for the GelMA_1G hydrogels, respectively, due to the chaotropic property, but subsequently increases to about 139.2 Å, 214.5 and 210.0 Å for the GelMA_3G, GelMA_5G and GelMA_10G, respectively, due to more extensive aggregation of the building blocks. The latter effect is discussed in more detail below.

The chaotropic properties of GdmCl also have an impact on the lower-level structure of the building blocks that construct the network with greater length. This local structure in the GelMA-based hydrogel is reflected by the intensity profile in the high q range ($q = 0.05$–0.3 Å^{-1}) in Fig. 5a. In this region, the parameters P_2 and R_{g2} are used to describe the fractal dimension and radius of gyration of the building block, respectively. Thus, the GelMA_0G hydrogel exhibits a P_2 value of approximately 2.4, indicating that the building block can be represented by a blob composed of locally branched or network chains. With the addition of GdmCl to the GelMA precursor solution, however, the self-crosslinking of GelMA is dissociated due to the chaotropic properties of GdmCl. Consequently, as the GdmCl concentration increases from 1 to 10 wt%, the P_2 value of the hydrogel approaches 2.0, corresponding to the fractal dimension of a linear Gaussian chain. Meanwhile, the R_{g2} value decreases from 24.6 for the GelMA_0G to 23.2, 22.5, 21.5, and 20.0 Å for the GelMA_1G, GelMA_3G, GelMA_5G, and GelMA_10G, respectively, due to the intermolecular hydrogen bonding interactions between the GelMA polymer and Gdm cations.

The two-level structure of the GelMA-based hydrogel is shown schematically in Fig. 6, where the lengthier fractal network characterized by the R_{g1} value is formed by local segmental association. This network can be visualized as being composed of interconnected blobs that are characterized by the R_{g2} value. The latter value also represents the mesh size of the network. A comparison with the results in Fig. 4d indicates that the increase in the Seebeck coefficient of the GelMA-based TGC with the increased concentration of GdmCl corresponds to a decrease in the mesh size. This is because the smaller mesh restricts the transfer of ion-induced crystals, thus leading to a larger concentration difference between the hot and cold sides of the cell. However, a dramatic decrease in the Seebeck coefficient is observed in the case of the GelMA_10G, which suggests that the quasi solid-state GdmCl-containing thermogalvanic system exhibits a critical mesh size. This is estimated to be around 20.0–21.5 Å. Once the mesh size falls below this critical value (e.g., in the GelMA_10G), the transfer of crystals and redox couples becomes increasingly difficult. This limitation hinders the enhancement of the Seebeck coefficient, thereby resulting in a decrease in the S value.

Notably, the R_{g2} and P_2 values of the GelMA_5G TGC remain more-or-less unchanged before and after the soaking process (Fig. 5c), i.e., $R_{g2} = 21.5$ and 21.2 Å, and $P_2 = 2.0$. This suggests that the introduction of the redox couple does not significantly alter the local structure of the GelMA_5G hydrogel. With introducing the higher content of GdmCl in GelMA (i.e., GelMA_5G hydrogels), one
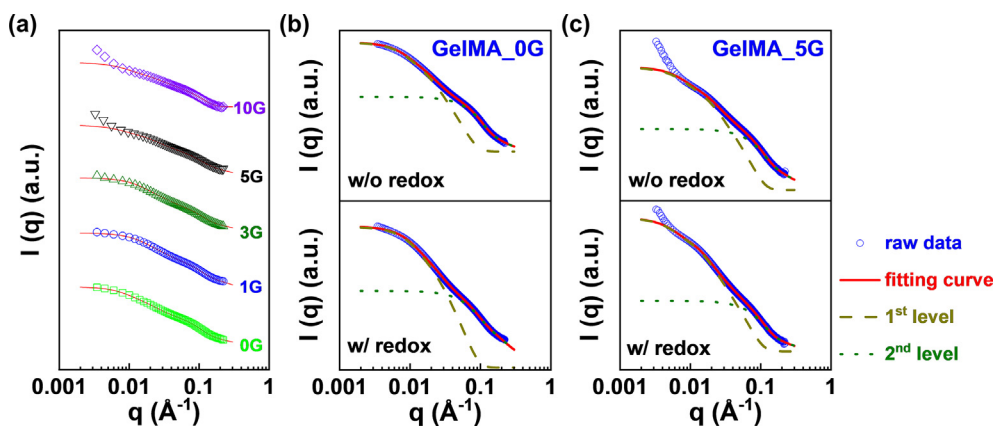

Fig. 5. (a) The SAXS profiles and fitting results of the various GelMA-based hydrogels. (b and c) the SAXS patterns of the GelMA_0G hydrogel (b) and the GelMA_5G hydrogel (c) before and after soaking in the precursor solution. The dashed line and the dotted line represent the respective 1st and 2nd level fitting results according to the Beaucage model.
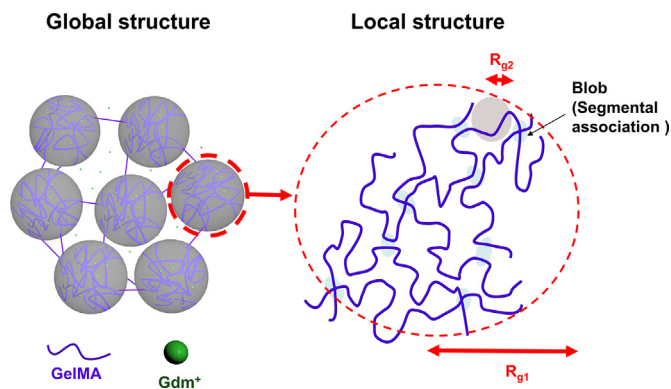
Fig. 6. A schematic diagram of the nanostructure of the GelMA-based hydrogel according to the Beaucage model, showing a cluster formed by the aggregation of polymer chains via local segmental association.

part of Gdm$^+$ is interact with GelMA polymer and the other non-interacted Gdm$^+$ would well distribute in the hydrogels. When the GelMA_5G hydrogel is immersed in the Fe(CN)$_6^{3-}$/Fe(CN)$_6^{4-}$ solution, the redox couple will interact with the residual Gdm$^+$ instead of GelMA polymers due to the strong interaction between the chaotropic cations and anions (Gdm$^+$ and Fe(CN)$_6^{3-}$/Fe(CN)$_6^{4-}$, respectively), in which screens the chaotropic effect between the redox couple and GelMA polymer, thereby maintaining the original nanostructure. The screening effect of this chaotropic effect can also be proved by the redox + G TGCs. The P_2 and R_{g2} values of redox + G TGCs remain unchanged before and after the soaking process of GelMA-0G hydrogels (Fig. S8 and Table S1). This phenomenon is due to the formation of the strong interaction between Gdm$^+$ and Fe(CN)$_6^{3-}$/Fe(CN)$_6^{4-}$ in the mixed redox solution. There is no additional Gdm$^+$ could interact with the GelMA polymers, and therefore P_2 and R_{g2} values are unchanged. By contrast, a clear change is observed in the GelMA_0G system after introducing the redox couple without Gdm$^+$ (Fig. 5b). Specifically, the local conformation of the chains within the blobs of GelMA_0G TGC shifts towards a Gaussian coil, as indicated by the change in the P_2 value from 2.4 to 2.0. Additionally, the R_{g2} value is seen to increase from 24.6 to 25.2 Å due to the chaotropic properties of Fe(CN)$_6^{3-}$ and Fe(CN)$_6^{4-}$, which increase the mesh size by disrupting the intermolecular interactions between the GelMA polymer chains in the GelMA_0G TGC. Based on these findings, it can be concluded that the introduction of GdmCl exerts a dual effect on the GelMA-based TGCs, involving both its interaction with the redox couple and its ability to control the mesh size of the hydrogel. These combined

effects ultimately contribute to the enhancement of the Seebeck coefficient.

The TGC with the highest Seebeck coefficient, i.e., the GelMA_5G TGC, was used to fabricate a flexible and wearable TEG. As shown in Fig. 7a and b, the TEG device consisted of three TGCs connected in series with nickel foils. The output characteristics of the TEG device under three different temperature gradients (ΔT) between the electrodes are shown in Fig. 7c. Here, it can be seen that the open-circuit voltage (V_{oc}) increases from 320.85 to 683.94 mV, and the maximum output power (W_{max}) increases from 4.01 to 23.94 μW, as ΔT increases from 5.1 to 10.3 °C. At the same time, the short-circuit current (I_{sc}) is seen to increase from 50 to 140 μA. The measured W_{max} values are in good agreement with the theoretically calculated values given by the formula $W_{max} = I_{sc} \times V_{oc}/4$. Specifically, at ΔT values of 5.1 °C and 10.3 °C, the calculated W_{max} values are 4.00 and 23.93 μW, respectively. Besides, the maximum power density (P_{max}) increases from 0.02 to 0.1 W m^{-2}, and the temperature-insensitive power density (i.e., $P_{max}/(\Delta T)^2$ value) is increases from 713 to 1064 μW m^{-2} K^{-2}, as ΔT increases from 5.1 to 10.3 °C (Fig. S9).

The practical application of the GelMA_5G TGC is demonstrated in Fig. 8a, where a prototype TEG device is worn on the forearm. Moreover, when the ΔT is measured using a thermal camera, the device is shown to generate a V_{oc} of approximately 218 mV at a ΔT of 3.5 °C between the human skin and the ambient environment. These results demonstrate the promising application potential of GelMA_5G TGC for harvesting low-grade thermal energy in wearable devices. The high Seebeck coefficient and the ability to generate significant voltage and power outputs make this device suitable for capturing and utilizing thermal energy in various practical scenarios. Moreover, the very large output voltage characteristics of the GelMA_5G TGC are well-suited for driving low-current electronic devices. This is demonstrated in Fig. 8c and d, where an array of 9 TGC units generates an output voltage of about 1.62 V at a ΔT of approximately 9 °C between the ambient environment and the hotplate. This voltage is sufficient to directly power a light-emitting diode (LED) without the need for a boosting driver. It is worth noting that the higher Seebeck coefficient of the TGC decreases the number of units required to achieve the same output voltage when connected in series. This simplifies the manufacturing process and improves the overall feasibility of the wearable thermoelectric device. However, the TEG device has a relatively lower output current, which may be attributed to poor electrode-to-cell contact. This issue can be addressed in future work by using carbon-based electrodes and implementing encapsulation techniques to enhance the contact between the electrodes and the TGCs.
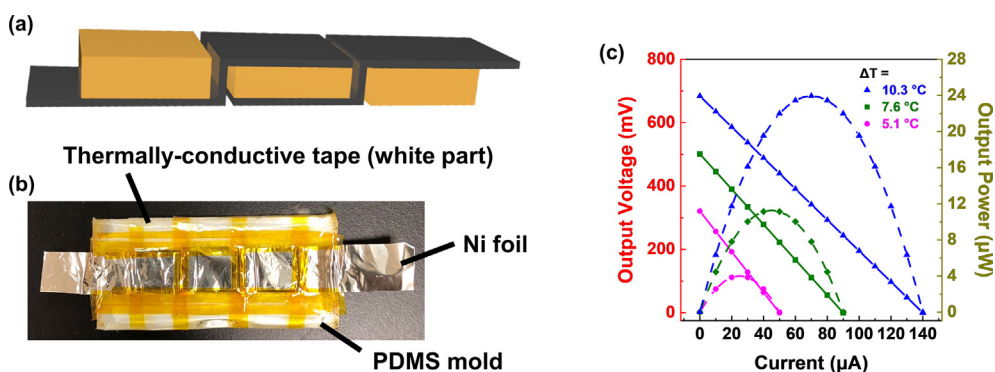

Fig. 7. (a) A schematic side view of the TEG device connected using Ni foil. (b) A photographic image of the 3-unit TEG device. (c) The output characteristics of the 3-unit TEG device measured under varying ΔT.
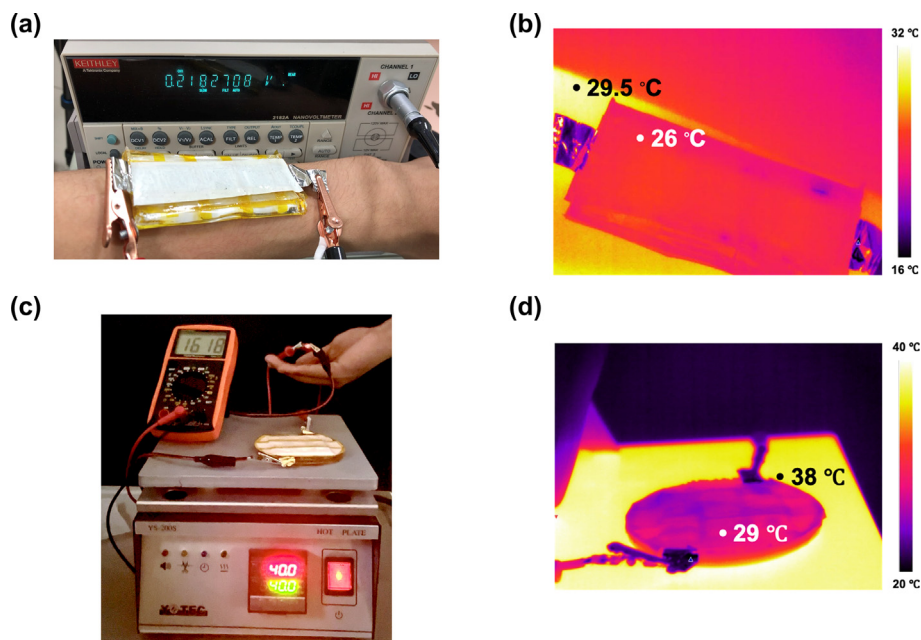
Fig. 8. (a) A demonstration of TEG device worn on the forearm, along with the output voltage due to the temperature difference between the human skin and the ambient environment ($\Delta T \sim 3.5\ °C$). (b) A thermal image showing the temperature distribution of the 3-unit TEG device. (c) A demonstration of the 9-unit TEG device capable of directly powering an LED without the need for additional voltage boosting. (d) A thermal image showing the temperature distribution of the 9-unit TEG device.

4. Conclusions

Herein, gelatin methacryloyl (GelMA)-based hydrogels were successfully fabricated and modified with guanidium chloride (GdmCl) to generate a thermoelectric system with a remarkable Seebeck coefficient. The incorporation of GdmCl not only improved the mechanical properties of the hydrogels, but also significantly improved the Seebeck coefficient, achieving a remarkable value of 21.6 mV K^{-1} when 5 wt% GdmCl was used (GelMA_5G). Further, the small angle X-ray scattering (SAXS) analysis indicated that the introduction of GdmCl induces alterations in the nanostructure of the hydrogel, thereby resulting in the formation of a lengthier network structure, and enabling control over the mesh size within the network. Moreover, a prototype TEG device consisting of interconnected GelMA_5G TGCs exhibited an output voltage of approximately 1.62 V when subjected to a temperature gradient (ΔT) of around 9 °C. Notably, this output voltage was sufficient to directly power an LED light without requiring additional voltage boosting drivers. The combined effects of GdmCl modification and the simplified fabrication process highlight the potential application of the GelMA_5G TGC in low-grade thermal energy harvesting, particularly for wearable devices.

CRediT authorship contribution statement

Shao-Huan Hong: Writing — review and editing, Writing — original draft, Visualization, Validation, Methodology, Investigation, Formal analysis, Data curation, Conceptualization. **Ching-Chieh Hsu:** Visualization, Validation, Investigation, Data curation. **Tai-Hung Liu:** Methodology, Investigation, Formal analysis, Conceptualization. **Tai-Chou Lee:** Resources. **Shih-Huang Tung:** Formal analysis, Data curation. **Hsin-Lung Chen:** Methodology, Formal analysis, Data curation. **Jiashing Yu:** Supervision, Resources, Methodology, Conceptualization. **Cheng-Liang Liu:** Writing — review and editing, Writing — original draft, Supervision, Resources, Project administration, Funding acquisition, Conceptualization.

Declaration of competing interest

The authors declare the following financial interests/personal relationships which may be considered as potential competing interests: Cheng-Liang Liu and Jiashing Yu reports financial support was provided by National Science and Technology Council. Cheng-Liang Liu reports was provided by Ministry of Education. Cheng-Liang Liu reports financial support was provided by National Taiwan University.

Data availability

Data will be made available on request.

Appendix A. Supplementary data

Supplementary data to this article can be found online at https://doi.org/10.1016/j.mtener.2024.101546.

References

[1] L. Chen, G. Msigwa, M. Yang, A.I. Osman, S. Fawzy, D.W. Rooney, P.-S. Yap, Strategies to achieve a carbon neutral society: a review, Environ. Chem. Lett. 20 (2022) 2277–2310, https://doi.org/10.1007/s10311-022-01435-8.

[2] Z. Su, M. Zhang, P. Xu, Z. Zhao, Z. Wang, H. Huang, T. Ouyang, Opportunities and strategies for multigrade waste heat utilization in various industries: a recent review, Energy Convers. Manag. 229 (2021) 113769, https://doi.org/10.1016/j.enconman.2020.113769.

[3] H. Kim, K.R. Pyun, M.-T. Lee, H.B. Lee, S.H. Ko, Recent advances in sustainable wearable energy devices with nanoscale materials and macroscale structures, Adv. Funct. Mater. 32 (2022) 2110535, https://doi.org/10.1002/adfm.202110535.

[4] S. Zhang, Z. Wu, Z. Liu, Z. Hu, An emerging energy Technology: self-uninterrupted electricity power harvesting from the sun and cold space, Adv. Energy Mater. 13 (2023) 2300260, https://doi.org/10.1002/aenm.202300260.

[5] Y. Jia, Q. Jiang, H. Sun, P. Liu, D. Hu, Y. Pei, W. Liu, X. Crispin, S. Fabiano, Y. Ma, Y. Cao, Wearable thermoelectric materials and devices for self-powered electronic systems, Adv. Mater. 33 (2021) 2102990, https://doi.org/10.1002/adma.202102990.

[6] Q. Yan, M.G. Kanatzidis, High-performance thermoelectrics and challenges for practical devices, Nat. Mater. 21 (2022) 503–513, https://doi.org/10.1038/s41563-021-01109-w.

[7] X.-L. Shi, W.-Y. Chen, T. Zhang, J. Zou, Z.-G. Chen, Fiber-based thermoelectrics for solid, portable, and wearable electronics, Energy Environ. Sci. 14 (2021) 729–764, https://doi.org/10.1039/D0EE03520C.

[8] L. Li, W.-D. Liu, Q. Liu, Z.-G. Chen, Multifunctional wearable thermoelectrics for personal thermal management, Adv. Funct. Mater. 32 (2022) 2200548, https://doi.org/10.1002/adfm.202200548.

[9] N. Toshima, Recent progress of organic and hybrid thermoelectric materials, Synth. Met. 225 (2017) 3–21, https://doi.org/10.1016/j.synthmet.2016.12.017.

[10] M. Massetti, F. Jiao, A.J. Ferguson, D. Zhao, K. Wijeratne, A. Würger, J.L. Blackburn, X. Crispin, S. Fabiano, Unconventional thermoelectric materials for energy harvesting and sensing applications, Chem. Rev. 121 (2021) 12465–12547, https://doi.org/10.1021/acs.chemrev.1c00218.

[11] Y. Liu, H. Wang, P.C. Sherrell, L. Liu, Y. Wang, J. Chen, Potentially wearable thermo-electrochemical cells for body heat harvesting: from mechanism, materials, strategies to applications, Adv. Sci. 8 (2021) 2100669, https://doi.org/10.1002/advs.202100669.

[12] T. Cao, X.-L. Shi, Z.-G. Chen, Advances in the design and assembly of flexible thermoelectric device, Prog. Mater. Sci. 131 (2023) 101003, https://doi.org/10.1016/j.pmatsci.2022.101003.

[13] J. He, T.M. Tritt, Advances in thermoelectric materials research: looking back and moving forward, Science 357 (2017) eaak9997, https://doi.org/10.1126/science.aak9997.

[14] J. Duan, G. Feng, B. Yu, J. Li, M. Chen, P. Yang, J. Feng, K. Liu, J. Zhou, Aqueous thermogalvanic cells with a high Seebeck coefficient for low-grade heat harvest, Nat. Commun. 9 (2018) 5146, https://doi.org/10.1038/s41467-018-07625-9.

[15] X. He, H. Sun, Z. Li, X. Chen, Z. Wang, Y. Niu, J. Jiang, C. Wang, Redox-induced thermocells for low-grade heat harvesting: mechanism, progress, and their applications, J. Mater. Chem. A 10 (2022) 20730–20755, https://doi.org/10.1039/D2TA05742E.

[16] H. Zhou, T. Yamada, N. Kimizuka, Supramolecular thermo-electrochemical cells: enhanced thermoelectric performance by host–guest complexation and salt-induced crystallization, J. Am. Chem. Soc. 138 (2016) 10502–10507, https://doi.org/10.1021/jacs.6b04923.

[17] K. Kim, J. Kang, H. Lee, Hybrid thermoelectrochemical and concentration cells for harvesting low-grade waste heat, Chem. Eng. J. 426 (2021) 131797, https://doi.org/10.1016/j.cej.2021.131797.

[18] Z. Lei, W. Gao, P. Wu, Double-network thermocells with extraordinary toughness and boosted power density for continuous heat harvesting, Joule 5 (2021) 2211–2222, https://doi.org/10.1016/j.joule.2021.06.003.

[19] P. Yang, K. Liu, Q. Chen, X. Mo, Y. Zhou, S. Li, G. Feng, J. Zhou, Wearable thermocells based on gel electrolytes for the utilization of body heat, Angew. Chem. Int. Ed. 55 (2016) 12050–12053, https://doi.org/10.1002/anie.201606314.

[20] L. Jin, G.W. Greene, D.R. MacFarlane, J.M. Pringle, Redox-active quasi-solid-state electrolytes for thermal energy harvesting, ACS Energy Lett. 1 (2016) 654–658, https://doi.org/10.1021/acsenergylett.6b00305.

[21] S. Sun, M. Li, X.-L. Shi, Z.-G. Chen, Advances in ionic thermoelectrics: from materials to devices, Adv. Energy Mater. 13 (2023) 2203692, https://doi.org/10.1002/aenm.202203692.

[22] S. Pu, Y. Liao, K. Chen, J. Fu, S. Zhang, L. Ge, G. Conta, S. Bouzarif, T. Cheng, X. Hu, K. Liu, J. Chen, Thermogalvanic hydrogel for synchronous evaporative cooling and low-grade heat energy harvesting, Nano Lett. 20 (2020) 3791–3797, https://doi.org/10.1021/acs.nanolett.0c00800.

[23] B. Yu, W. Yang, J. Li, W. Xie, H. Jin, R. Liu, H. Wang, X. Zhuang, B. Qi, S. Liu, L. Huang, B. Hu, J. Duan, J. Zhou, Heat-triggered high-performance thermocells enable a self-powered forest fire alarm, J. Mater. Chem. A 9 (2021) 26119–26126, https://doi.org/10.1039/D1TA06793A.

[24] Z. Lei, W. Gao, W. Zhu, P. Wu, Anti-fatigue and highly conductive thermocells for continuous electricity generation, Adv. Funct. Mater. 32 (2022) 2201021, https://doi.org/10.1002/adfm.202201021.

[25] W. Gao, Z. Lei, C. Zhang, X. Liu, Y. Chen, Stretchable and freeze-tolerant organohydrogel thermocells with enhanced thermoelectric performance continually working at subzero temperatures, Adv. Funct. Mater. 31 (2021) 2104071, https://doi.org/10.1002/adfm.202104071.

[26] Y. Li, Q. Li, X. Zhang, B. Deng, C. Han, W. Liu, 3D hierarchical electrodes boosting ultrahigh power output for gelatin-KCl-FeCN$^{4-/3-}$ ionic thermo-electric cells, Adv. Energy Mater. 12 (2022) 2103666, https://doi.org/10.1002/aenm.202103666.

[27] Y. Liu, S. Zhang, Y. Zhou, M.A. Buckingham, L. Aldous, P.C. Sherrell, G.G. Wallace, G. Ryder, S. Faisal, D.L. Officer, S. Beirne, J. Chen, Advanced wearable thermocells for body heat harvesting, Adv. Energy Mater. 10 (2020) 2002539, https://doi.org/10.1002/aenm.202002539.

[28] C. Tian, C. Bai, T. Wang, Z. Yan, Z. Zhang, K. Zhuo, H. Zhang, Thermogalvanic hydrogel electrolyte for harvesting biothermal energy enabled by a novel redox couple of $SO_{4/3}^{2-}$ ions, Nano. Energy 106 (2023) 108077, https://doi.org/10.1016/j.nanoen.2022.108077.

[29] C.-G. Han, X. Qian, Q. Li, B. Deng, Y. Zhu, Z. Han, W. Zhang, W. Wang, S.-P. Feng, G. Chen, W. Liu, Giant thermopower of ionic gelatin near room temperature, Science 368 (2020) 1091–1098, https://doi.org/10.1126/science.aaz5045.

[30] Y. Liu, Q. Zhang, G.O. Odunmbaku, Y. He, Y. Zheng, S. Chen, Y. Zhou, J. Li, M. Li, K. Sun, Solvent effect on the Seebeck coefficient of Fe^{2+}/Fe^{3+} hydrogel thermogalvanic cells, J. Mater. Chem. A 10 (2022) 19690–19698, https://doi.org/10.1039/D1TA10508F.

[31] D. Zhang, Y. Mao, F. Ye, Q. Li, P. Bai, W. He, R. Ma, Stretchable thermogalvanic hydrogel thermocell with record-high specific output power density enabled by ion-induced crystallization, Energy Environ. Sci. 15 (2022) 2974–2982, https://doi.org/10.1039/D2EE00738J.

[32] Y. Li, Q. Li, X. Zhang, J. Zhang, S. Wang, L. Lai, K. Zhu, W. Liu, Realizing record-high output power in flexible gelatin/GTA-KCl-FeCN$^{4-/3-}$ ionic thermoelectric cells enabled by extending the working temperature range, Energy Environ. Sci. 15 (2022) 5379–5390, https://doi.org/10.1039/D2EE02792E.

[33] Y. Zhou, S. Zhang, M.A. Buckingham, L. Aldous, S. Beirne, C. Wu, Y. Liu, G. Wallace, J. Chen, Novel porous thermosensitive gel electrolytes for wearable thermo-electrochemical cells, Chem. Eng. J. 449 (2022) 137775, https://doi.org/10.1016/j.cej.2022.137775.

[34] L. Jiang, S. Horike, M. Mukaida, K. Kirihara, K. Seki, Q. Wei, High-performance isotropic thermo-electrochemical cells using agar-gelled ferricyanide/ferrocyanide/guanidinium, Global Chall. 7 (2023) 2200207, https://doi.org/10.1002/gch2.202200207.

[35] Z. Li, S. Zhang, Y. Chen, H. Ling, L. Zhao, G. Luo, X. Wang, M.C. Hartel, H. Liu, Y. Xue, R. Haghniaz, K. Lee, W. Sun, H. Kim, J. Lee, Y. Zhao, Y. Zhao, S. Emaminejad, S. Ahadian, N. Ashammakhi, M.R. Dokmeci, Z. Jiang, A. Khademhosseini, Gelatin methacryloyl-based tactile sensors for medical wearables, Adv. Funct. Mater. 30 (2020) 2003601, https://doi.org/10.1002/adfm.202003601.

[36] B. Liu, Y. Wang, Y. Miao, X. Zhang, Z. Fan, G. Singh, X. Zhang, K. Xu, B. Li, Z. Hu, M. Xing, Hydrogen bonds autonomously powered gelatin methacrylate hydrogels with super-elasticity, self-heal and underwater self-adhesion for sutureless skin and stomach surgery and E-skin, Biomaterials 171 (2018) 83–96, https://doi.org/10.1016/j.biomaterials.2018.04.023.

[37] K.-F. Yu, T.-Y. Lu, Y.-C.E. Li, K.-C. Teng, Y.-C. Chen, Y. Wei, T.-E. Lin, N.-C. Cheng, J. Yu, Design and synthesis of stem cell-laden keratin/glycol chitosan methacrylate bioinks for 3D bioprinting, Biomacromolecules 23 (2022) 2814–2826, https://doi.org/10.1021/acs.biomac.2c00191.

[38] T.C. Lai, J. Yu, W.B. Tsai, Gelatin methacrylate/carboxybetaine methacrylate hydrogels with tunable crosslinking for controlled drug release, J. Mater. Chem. B 4 (2016) 2304–2313, https://doi.org/10.1039/C5TB02518D.

[39] E. Hoch, C. Schuh, T. Hirth, G.E.M. Tovar, K. Borchers, Stiff gelatin hydrogels can be photo-chemically synthesized from low viscous gelatin solutions using molecularly functionalized gelatin with a high degree of methacrylation, J. Mater. Sci. Mater. Med. 23 (2012) 2607–2617, https://doi.org/10.1007/s10856-012-4731-2.

[40] K. Yue, G. Trujillo-de Santiago, M.M. Alvarez, A. Tamayol, N. Annabi, A. Khademhosseini, Synthesis, properties, and biomedical applications of gelatin methacryloyl (GelMA) hydrogels, Biomaterials 73 (2015) 254–271, https://doi.org/10.1016/j.biomaterials.2015.08.045.

[41] J. Vasudevan, C.T. Lim, J.G. Fernandez, Cell migration and breast cancer metastasis in biomimetic extracellular matrices with independently tunable stiffness, Adv. Funct. Mater. 30 (2020) 2005383, https://doi.org/10.1002/adfm.202005383.

[42] D.F.S. Fonseca, P.C. Costa, I.F. Almeida, P. Dias-Pereira, I. Correia-Sá, V. Bastos, H. Oliveira, C. Vilela, A.J.D. Silvestre, C.S.R. Freire, Swellable gelatin methacryloyl microneedles for extraction of interstitial skin fluid toward minimally invasive monitoring of urea, Macromol. Biosci. 20 (2020) 2000195, https://doi.org/10.1002/mabi.202000195.

[43] D. Sun, Y. Feng, S. Sun, J. Yu, S. Jia, C. Dang, X. Hao, J. Yang, W. Ren, R. Sun, C. Shao, F. Peng, Transparent, self-adhesive, conductive organohydrogels with fast gelation from lignin-based self-catalytic system for extreme environment-resistant triboelectric nanogenerators, Adv. Funct. Mater. 32 (2022) 2201335, https://doi.org/10.1002/adfm.202201335.

[44] A. Barth, Infrared spectroscopy of proteins, Biochim. Biophys. Acta Bioenerg. 1767 (2007) 1073–1101, https://doi.org/10.1016/j.bbabio.2007.06.004.

[45] O.D. Bonner, C.F. Jordan, The infrared and Raman spectra of guanidinium salts, Spectrochim. Acta A Mol. Biomol. 32 (1976) 1243–1246, https://doi.org/10.1016/0584-8539(76)80316-9.

[46] B. Yu, J. Duan, H. Cong, W. Xie, R. Liu, X. Zhuang, H. Wang, B. Qi, M. Xu, Z.L. Wang, J. Zhou, Thermosensitive crystallization–boosted liquid thermocells for low-grade heat harvesting, Science 370 (2020) 342–346, https://doi.org/10.1126/science.abd6749.

[47] L. Liu, D. Zhang, P. Bai, Y. Mao, Q. Li, J. Guo, Y. Fang, R. Ma, Strong tough thermogalvanic hydrogel thermocell with extraordinarily high thermoelectric performance, Adv. Mater. 35 (2023) 2300696, https://doi.org/10.1002/adma.202300696.

[48] G. Beaucage, Approximations leading to a unified exponential/power-law approach to small-angle scattering, J. Appl. Crystallogr. 28 (1995) 717–728, https://doi.org/10.1107/S0021889895005292.

[49] Y.-C. Li, K.-B. Chen, H.-L. Chen, C.-S. Hsu, C.-S. Tsao, J.-H. Chen, S.-A. Chen, Fractal aggregates of conjugated polymer in solution state, Langmuir 22 (2006) 11009–11015, https://doi.org/10.1021/la0612769.

[50] C.D. Putnam, M. Hammel, G.L. Hura, J.A. Tainer, X-ray solution scattering (SAXS) combined with crystallography and computation: defining accurate macromolecular structures, conformations and assemblies in solution, Q. Rev. Biophys. 40 (2007) 191–285, https://doi.org/10.1017/S0033583507004635.